Available online at www.sciencedirect.com
SCIENCE DIRECT®
Continental Shelf Research 25 (2005) 2107–2121
CONTINENTAL SHELF RESEARCH
www.elsevier.com/locate/csr

Japan/East Sea model predictability

Peter C. Chu[a,*], Chin-Lung Fang[a], Chang S. Kim[b]

[a]*Naval Ocean Analysis and Prediction Laboratory, Department of Oceanography, Naval Postgraduate School, Monterey, CA, USA*
[b]*Korea Ocean Research and Development Institute, Ansan 425-170, South Korea*

Available online 29 September 2005

Abstract

Three major input uncertainties (initial velocity field, open boundary conditions, and atmospheric forcing) limit the ocean modeling capability. The Princeton Ocean Model (POM) implemented to the Japan/East Sea (JES) is used to investigate the ocean predictability due to the input uncertainties. Two-step (pre-simulation and simulation) initialization is used to obtain ''standard initial velocity''. Twelve experiments are conducted with one control run and 11 sensitivity runs. The control run is to integrate POM–JES from the ''standard initial velocity'' with the lateral transport (unperturbed) and the daily surface wind stress, net heat flux, and fresh-water flux interpolated from the COADS monthly mean data (unperturbed). The sensitivity runs are to integrate POM–JES with replaced initial velocity fields (with or without diagnostic initialization), and noisy winds and lateral boundary transports.

Model uncertainty due to uncertain input data (initial velocity, winds, and lateral boundary transport) is significant. Level independent relative root mean square error for the whole JES is 0.2–0.5 for uncertain initial velocity field, 0.19 for uncertain surface winds with 0.5 m/s noise, and 0.20 for uncertain lateral transport with 5% noise. The maximum level dependent relative root mean square error reaches 0.6 at the surface for uncertain winds (0.5 m/s noise), and 0.18 at the bottom for uncertain lateral transport (5% noise). Model uncertainty reduces with time for uncertain initial velocity field, oscillates with an evident error growing trend for uncertain winds, and oscillates with no evident error growing trend for uncertain lateral transport. Furthermore, there is no difference using and not using the diagnostic (velocity) initialization and no difference in choosing periods (30–90 days) for diagnostic initialization.
Published by Elsevier Ltd.

1. Introduction

Three major difficulties limit the ocean modeling capability. First, the initial velocity field is usually not available due to insufficient velocity observations. A diagnostic initialization is widely used to determine the initial velocity. The model is integrated from known T, S, such as climatological data (T_c, S_c) and zero velocity fields, while holding T_c and S_c unchanged. After a period (about 30 days) of the diagnostic run, the velocity field (V_c) is established, and T_c, S_c and V_c fields are treated as the initial conditions for numerical prognostic modeling. Recently, Chu and Lan (2003) pointed out that during the diagnostic initialization period, unrealistic heat and salt 'source/sink' terms are generated at each time step.

Second, atmospheric forcing function is uncertain. This is largely due to lack of meteorological observations over the ocean surface. For example, Chu et al. (1999) found significant difference in wind forcing over the South China Sea during the lifetime of tropical cyclone Ernie (November 4–18, 1996)

*Corresponding author.
E-mail address: chu@nps.navy.mil (P.C. Chu).

0278-4343/$ - see front matter Published by Elsevier Ltd.
doi:10.1016/j.csr.2005.03.006

between NASA's Scatterometer (NSCAT) and NOAA's National Centers for Environmental Prediction (NCEP) winds. The root-mean-square difference increased from 3.6 m s^{-1} on November 1 to a maximum value of 6.7 m s^{-1} on November 4, 1996, which was the day the boundary current was strongest, fluctuating afterward between 6.7 and 2.7 m s^{-1}.

Third, lateral boundary condition is uncertain in regional ocean models (Chu et al., 1997). At open boundaries where the numerical grid ends, the fluid motion should be unrestricted since ideal open boundaries are transparent to motions. Two approaches, local-type and inverse-type, are available for determining open boundary condition (OBC). The local-type approach determines the OBC from the solution of the governing equations near the boundary. The problem becomes selecting from a set of ad hoc OBCs. Since any ad hoc OBC will introduce noise into a numerical solution (Chapman, 1985), it is important to choose the best one from ad hoc OBCs for a particular ocean model. Without any ad hoc OBC, the inverse-type approach can determine the OBC from the "best" fit between model solutions and interior observations (Chu et al., 1997). However, both methods bring considerable errors in OBC.

Chu (1999) investigates two kinds of predictability in the Lorenz system: uncertain initial condition (first kind) and uncertain external forcing (second kind). Similarly, the first kind ocean model predictability is due to uncertain initial condition, and the second kind ocean model predictability is due to uncertain lateral boundary condition and atmospheric forcing. Most studies on ocean predictability have usually been focused on one particular type of model input uncertainty. A recent numerical experiment was designed to study the two kinds of predictability (Fang, 2003).

In this study, we investigate the two kinds of model predictability together using the Princeton Ocean Model (POM) implemented to the Japan/East Sea (JES). The rest of the paper is organized as follows. In Section 2, JES oceanography is described. In Section 3, POM is introduced. In Section 4, the experimental design is described. In Section 5, tanalysis methods are introduced. In Section 6, model errors due to input uncertainty are investigated. Finally, in Section 7, the conclusions are presented.

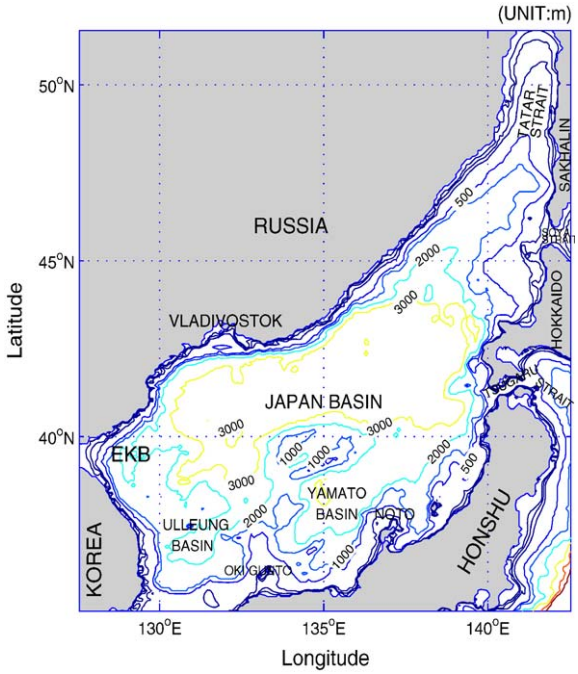

Fig. 1. The Japan/East Sea geography and bottom topography.

2. JES oceanography

The Japan Sea, known as the East Sea in Korea, has steep bottom topography (Fig. 1) that makes it a unique semi-enclosed ocean basin overlaid by pronounced monsoon surface winds. JES covers an area of 10^6 km^2. It has a maximum depth in excess of 3700 m, and is isolated from open oceans except for small (narrow and shallow) straits. JES connects with the North Pacific through the Korea/Tsushima and Tsugaru Straits and with the Okhotsk Sea through the Soya and Tatar Straits. In addition, JES contains three major basins called the Japan Basin (JB), Ulleung/Tsushima Basin (UTB), and Yamato Basin (YB); it also has a high central plateau called the Yamato Rise (YR). The JES is of great scientific interest as a miniature prototype ocean. Its basin-wide circulation pattern, boundary currents, Subpolar Front (SPF), mesoscale eddy activities and deepwater formation are similar to those in a large ocean.

2.1. Thermohaline structure

The thermohaline structure of JES has been studied by many investigators (Gong and Park, 1969; Isoda and Saitoh, 1993; Isoda et al.,

1991; Chu et al., 2001a, b; Gordon et al., 2002) using limited data sets. For example, after analyzing satellite infrared (IR) images and routine hydrographic survey data (by the Korea Fisheries Research and Development Agency) for the western part of the JES in the winter and the spring 1987, Isoda and Saitoh (1993) found that a small meander of a thermal front originates from the Korean/Tsushima Strait near the Korean coast gradually growing into an isolated warm eddy with a horizontal scale of 100 km. The warm eddy moves slowly northward from spring to summer.

Although the seasonal thermal variability on 150 m depth is weaker than on the surface, SPF still occurs at around 40°N consistently throughout the year, and it is located at almost the same location as at the surface. It divides the water masses with different characteristics. North of the SPF, the temperature is uniformly cold (1–3 °C) throughout the year. South of the SPF, the temperature changes from 5 to 9 °C. The SPF meandering at 131°E, 134°E, and 138°E forms several mesoscale eddies (Chu et al., 2001a, b). The SPF meandering near Okin Gunto (134 E) in spring was previously reported by Isoda and Saitoh (1993).

With limited data, Miyazaki (1953) found a low salinity layer in the SPF region. Later on Kim and Chung (1984) found very similar property in UTB which they called the JES Intermediate Water (JIW). After analyzing the comprehensive hydrographic data for the whole JES collected by the Japan Meteorological Agency, the Maizuru Marine Observatory, and the Hydrographic Department of the Japan Maritime Safety Agency, Senjyu (1999) demonstrates the existence of a salinity minimum (SMIN) layer (i.e., JIW) between the TWC Water and the JES Proper Water. The southwestern JES west of 132 °E is the upstream region of JIW. The lowest salinity and the highest oxygen concentration are found in the 38–40°N areas west of 132°E. The JIW takes two flow paths: an eastward flow along the SPF and a southward flow parallel with the Korean coast in the region west of 132°E. Analyzing the hydrographic collected from an international program, Circulation Research of the East Asian Marginal Seas (CREAMS), Kim and Kim (1999) discovered the high salinity water with high oxygen in the eastern JB (i.e., north of SPF) naming it the high salinity intermediate water (HSIW).

2.2. Current systems

Most of the nearly homogeneous water in the deep part of the basin is called the Japan Sea Proper Water (Moriyasu, 1972) and is of low temperature and low salinity. Above the Proper Water, the Tsushima Warm Current (TWC), dominating the surface layer, flows in from the East China Sea through the Korea/Tsushima Strait carrying warm water from the south. The Liman Cold Current (LCC) carries cool fresh surface water from the north and northeast (Seung and Kim, 1989; Holloway et al., 1995). The properties of this surface water are generally believed to be determined by the strong wintertime cooling coupled with fresh water input from the Amur River and the melting sea ice in Tatar Strait (Martin and Kawase, 1998). The LCC flows southward along the Russian coast, beginning at latitudes slightly north of Soya Strait, terminating off Vladivostok, and becoming the North Korean Cold Current (NKCC) after reaching the North Korean coast (Yoon, 1982).

Recently, Chu et al. (2001a, b) further reported the seasonal variation of the thermohaline structure and inverted circulation from the Navy's unclassified Generalized Digital Environmental Model (GDEM) temperature and salinity data on a $0.5^\circ \times 0.5^\circ$ grid using the *P*-vector method (Chu, 1995). The GDEM for the JES was built on 136,509 temperature and 52,572 salinity (1930–1997) historical profiles. A three-dimensional estimate of the absolute geostrophic velocity field was obtained from the GDEM temperature and salinity fields using the *P*-vector method (Fig. 2). Using the data collected from conductivity–temperature–depth (CTD) and acoustic Doppler current profilers (ADCP) measurements in the southwestern JES from March to June 1992, Shin et al. (1995, 1996) found a dipole structure of gyres with an anticyclonic eddy near the Korean coast and a cyclonic eddy in the UTB. Basic characteristics of current system were also recently modeled by Hogan and Hurlburt (2000) and Spall (2002).

2.3. Atmospheric forcing

The Asian monsoon strongly affects the thermal structure of the JES. During the winter monsoon season, a very cold northwest wind blows over the JES (Fig. 3a) as a result of the siberian high-pressure system with a mean surface wind speed between 10 and 15 m/s. By late April, numerous

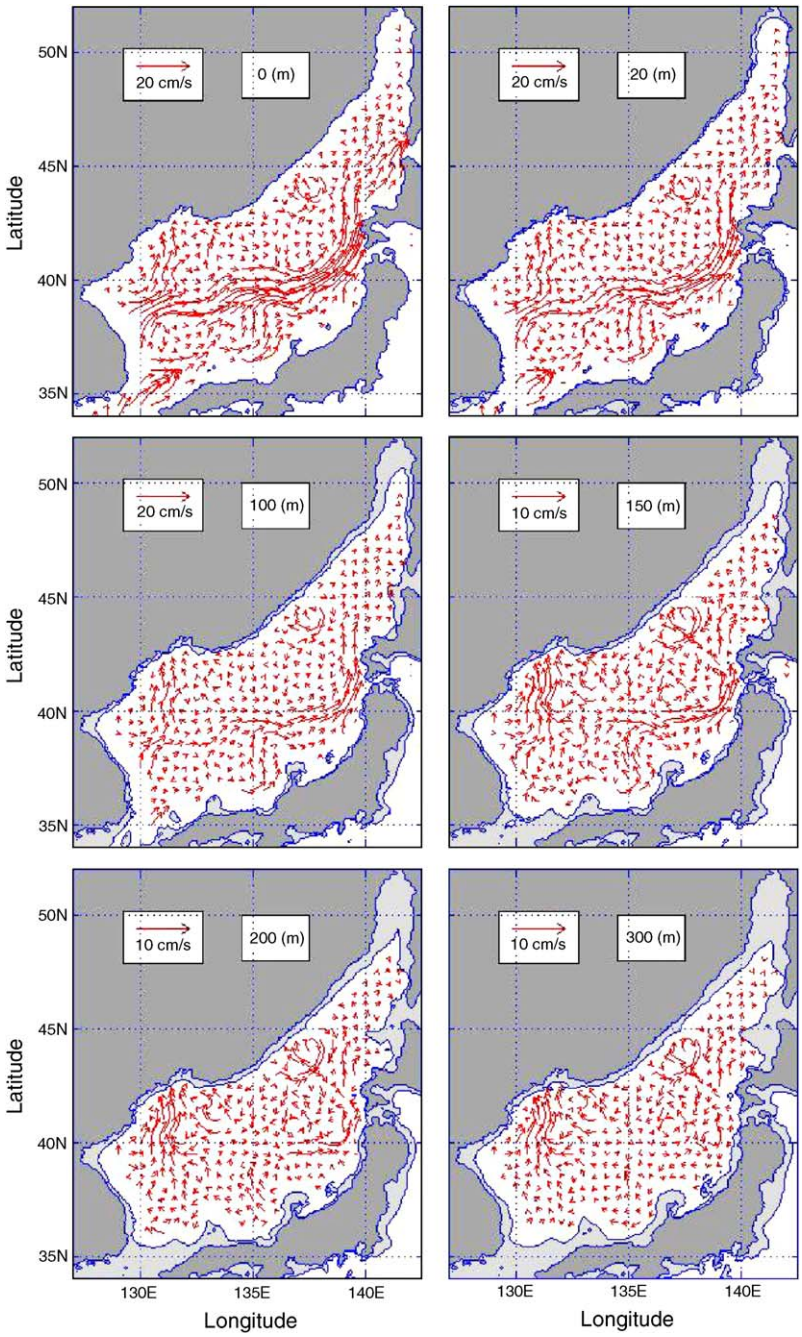

Fig. 2. Inverted annual mean velocity vectors at different depths: (a) 0, (b) 50 m, (c) 100 m, (d) 150 m, (e) 200 m, and (f) 300 m (from Chu et al., 2001a).

frontally generated events occur making late April and May highly variable in terms of wind speeds and the amount of clouds. During this period, storms originating in Mongolia may cause strong, warm westerlies (Fig. 3b). By late May and early June, a summer surface atmospheric low-pressure system begins to form over Asia. Initially, this low-pressure system is centered north of the Yellow Sea producing westerly winds. In late June, this low begins to migrate to the west setting up the southwest monsoon that dominates the summer months. The winds remain variable through June

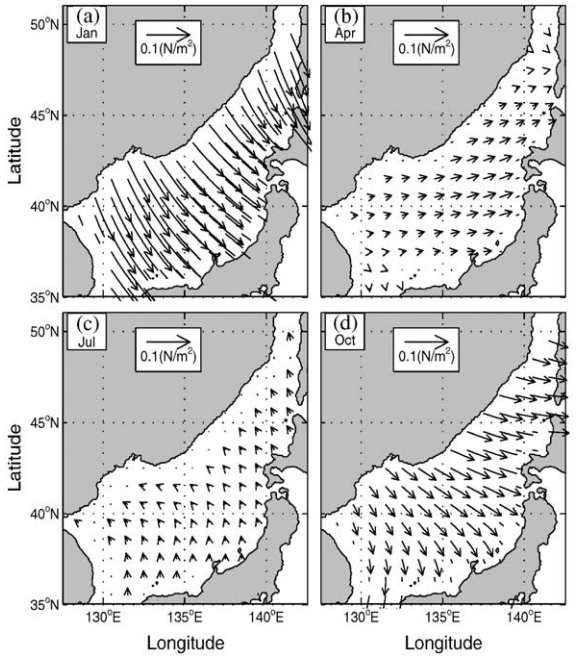

Fig. 3. Climatological wind stress from the COADS data.

until the Manchurian low-pressure system strengthens. Despite the very active weather systems, the mean surface wind speed over the JES in summer (Fig. 3c) is between 3 and 4 m/s, much weaker than in winter (Fig. 3a). By July, however, high pressure (the Bonin High) to the south and the low pressure over Manchuria produce southerly winds carrying warm, moist air over the East China Sea/Yellow Sea. In summer, warm air and strong downward net radiation stabilize the upper layer of the JES causing the surface mixed layer to shoal. October (Fig. 3d) is the beginning of the transition to winter conditions. The southerly winds weaken and the sea surface slope establishes its winter pattern.

3. Numerical ocean model

3.1. Model description

Coastal oceans and semi-enclosed seas are marked by extremely high spatial and temporal variability that challenges the existing predictive capabilities of numerical simulations. POM is a time-dependent, primitive equation circulation model rendered on a three-dimensional grid that includes realistic topography and a free surface (Blumberg and Mellor, 1987). Tidal forcing was not included in this application of the model, since high frequency variability of the circulation is not considered. River outflow is also not included. However, the seasonal variation in sea surface height, temperature, salinity, circulation, and transport are represented by the model. From a series of numerical experiments, the qualitative and quantitative effects of nonlinearity, wind forcing, and lateral boundary transport on the JES is analyzed, yielding considerable insight into the external factors affecting the regional oceanography.

Consequently, the model contains $181 \times 199 \times 23$ fixed grid points. The horizontal spacing is $5'$ latitude and longitude (approximately 5.77–7.59 km in the zonal direction and 9.265 km in the latitudinal direction) and there are 23 sigma levels in vertical coordinate. The model domain extends from 35.0° to 51.0°N, 127.0° to 142.0°E. The bottom topography (Fig. 1) is obtained from the Naval Oceanographic Office's Digital Bathymetry Data Base $5' \times 5'$ resolution (DBDB5). The horizontal friction and mixing are modeled using the Smagorinsky form with the coefficient chosen to be 0.2 for this application.

3.2. Surface forcing functions

The atmospheric forcing for the JES application of POM includes mechanical and thermohaline forcing. The wind forcing is depicted by

$$\rho_0 K_M \left(\frac{\partial u}{\partial z}, \frac{\partial v}{\partial z}\right)_{z=0} = (\tau_{0x}, \tau_{0y}), \tag{1}$$

where K_M is the vertical mixing coefficient for momentum, $(u,\ v)$ and $(\tau_{0x},\ \tau_{0y})$ are the two components of the water velocity and wind stress vectors, respectively. The wind stress at each time step is interpolated from monthly mean climatological wind stress from COADS (1945–1989), with a resolution of $1^\circ \times 1^\circ$. The COADS wind stress was interpolated into the model grid with a resolution of $5'$.

Surface thermohaline forcing is depicted by

$$K_H \frac{\partial \theta}{\partial z} = \alpha_1 \left(\frac{Q_H}{\rho C p}\right) + \alpha_2 C(\theta_{OBS} - \theta), \tag{2}$$

$$K_S \frac{\partial S}{\partial z} = -\alpha_1 F S + \alpha_2 (S_{OBS} - S), \tag{3}$$

where K_H and K_S are the vertical mixing coefficients for heat and salt, $(\theta,\ S)$ and $(\theta_{OBS},\ S_{OBS})$ are modeled and observed potential temperature and salinity, and c_p is the specific heat. $(Q_H,\ F)$ are net

heat and fresh water fluxes (downward positive). The parameters (α_1, α_2) are (0, 1) switchers: $\alpha_1 = 0$, $\alpha_2 = 1$, would specify the restoring forcing; $\alpha_1 = 1$, $\alpha_2 = 0$, would specify the flux forcing. The relaxation coefficient C is the reciprocal of the restoring time period for a unit volume of water.

3.3. Lateral boundary forcing

Boundary conditions for closed lateral boundaries, i.e., the modeled ocean bordered by land, were defined using a free-slip condition for velocity and a zero gradient condition for temperature and salinity. Thus, no advective or diffusive heat, salt or velocity fluxes occur through these boundaries. The radiation condition (local-type approach) is used to determine T, S at the open boundaries. When the water flows into the model domain, temperature and salinity at the open boundary are prescribed from observational data. When water flows out of the domain, the radiation condition was applied,

$$\frac{\partial}{\partial t}(\theta, S) + U_n \frac{\partial}{\partial n}(\theta, S) = 0, \tag{4}$$

where the subscript n denotes the direction normal to the boundary. The temperature and salinity values at the open boundaries are obtained from monthly mean climatological data such as the Navy's Generalized Digital Environmental Model (GDEM) data (Chu et al., 1998).

Volume transports at open boundaries are specified from historical data (Table 1). Positive (negative) values are referred to inflow (outflow). Warm water enters the JES through the Korea/Tsushima Strait with the TWC from the East China Sea and exits the JES through the Tsugaru and Soya straits. There is no evident volume transport through the Tatar Strait (Martin and Kawase, 1998), which was taken as 0 in this study. Recent estimate of the monthly mean volume transport, reported by Yi (1966), through the Korea/Tsushima Strait with the annual average of 1.3 Sv, a maximum of 2.2 Sv in October, and a minimum of 0.3 Sv in February. Bang et al. (1996) used the maximum inflow transport of about 3.5 Sv in August and minimum of 1.6 Sv in February, while Kim and Yoon (1996) used the mean value of 2.2 Sv with ±0.35 Sv with the maximum in mid-September and the minimum in mid-March. The total inflow transport through Korea/Tsushima Straits should be the same as the total outflow transport through the Tsugaru and Soya Straits. We assume that 75% (80% in Bang et al., 1996) of the total inflow transport should flow out of the JES through the Tsugaru Strait, and 25% (20% in Bang et al., 1996) through the Soya Strait. This ratio is adopted from the maximum volume transport through the Tsugaru Strait estimated by Toba et al. (1982), and through the Soya Strait estimated by Preller and Hogan (1998). The monthly volume transports through open boundaries are listed in Table 1.

Table 1
The bi-monthly variation of volume transport (unit: Sv, $1\,\text{Sv} = 10^6\,\text{m}^3/\text{s}$)

Month	Feb.	Apr.	Jun.	Aug.	Oct.	Dec.
Tatar strait (inflow)	0.05	0.05	0.05	0.05	0.05	0.05
Soya strait (outflow)	−0.1	−0.1	−0.4	−0.6	−0.7	−0.4
Tsugaru strait (outflow)	−0.25	−0.35	−0.85	−1.45	−1.55	−1.05
Tsushima strait (inflow)	0.3	0.4	1.2	2.0	2.2	1.4

3.4. Mode splitting

For computational efficiency, the mode splitting technique (Blumberg and Mellor, 1987) is applied with a barotropic time step of 25 s, based on the Courant–Friederichs–Levy computational stability (CFL) condition and the external wave speed; and a baroclinic time step of 900 s, based on the CFL condition and the internal wave speed.

3.5. Two-step initialization

Two-steps are used to obtain "standard initial velocity field" for the study: pre-simulation and simulation.

(a) *Pre-simulation step*: During the first step (restoring run), POM is integrated for 2 years from zero velocity and climatological annual mean temperature and salinity fields with the monthly mean surface wind stress from the COADS data and restoring-type surface thermohaline forcing ($\alpha_1 = 0$, $\alpha_2 = 1$) which is relaxed to surface monthly mean values.

(b) *Simulation stage*: The final states of the first step are taken as initial conditions for the second step (simulation run). During the simulation run, POM is integrated again for one and half years starting from Julian Day (JD)-1 to JD-180 of the second year using the flux forcing ($\alpha_1 = 1$, $\alpha_2 = 0$) with monthly mean surface wind stress

(τ_{0x}, τ_{0y}), net heat flux (Q_H), and net fresh-water flux (F) from the COADS data. The atmospheric forcing data are temporally interpolated into daily data. The final states of the simulation stage,

$$\mathbf{V}_0 = \mathbf{V}_{JD180}, \quad T_0 = T_{JD180}, \quad S_0 = S_{JD180}, \quad (5)$$

are taken as standard initial conditions for the numerical experiments.

4. Experimental design

4.1. Evaluation strategy

Ocean model output should be verified by the reality, which is represented approximately by observational (sampling) data with sufficient temporal and spatial coverage and resolution. Such a verification dataset is either not available or containing error. The initial and forcing data (wind and lateral transport) also contain error even the climatology. Difference between the model output and the observational data (if available) not only represents the model predictability but also the effect due to uncertain verification data.

In order to filter out the effect due to uncertain verification data and to quantify the uncertainty in initial and forcing data, a control run is designed with known initial condition, wind forcing, and lateral transport. The model input (initial and forcing) data are treated as 'accurate'. The model output data are taken as the 'reality' (i.e., the verification data without error).

Sensitivity runs are designed with quantified errors in initial condition (non-random error) or forcing data (random error). Comparison between the model output data and the 'realty' (i.e., the output data from the control run) quantifies the two kinds of the model predictability.

Twelve experiments are conducted with one control run and eleven sensitivity runs (Table 2) to investigate the model uncertainty caused by uncertain initial velocity fields, winds, and lateral boundary transports. The flux forcing ($\alpha_1 = 1$, $\alpha_2 = 0$) is used for these experiments.

4.2. Control run

The control run is to integrate POM–JES from the standard initial conditions (5) for 180 days (to JD-360) with the lateral transport shown in Table 1 (unperturbed) and the daily surface wind stress, net heat flux, and fresh-water flux interpolated from the COADS monthly mean data (unperturbed). Detailed information can be found in Chu et al. (2003).

Table 2
Summary of experimental design

Experiment	Property	Description
0	Control run	Section 4.1
1	Uncertain velocity initialization processes	Section 4.2
2		
3		
4		
5	Uncertain wind stress	Section 4.3
6		
7	Uncertain lateral boundary transport	Section 4.4
8		
9	Combination of uncertainty	Section 4.5
10		
11		

The simulated surface velocity field (Fig. 15 in Chu et al., 2003) coincides with earlier description of JES circulation presented in Section 2. Since this study is only interested in the model error caused by input uncertainty, we only provide rough description about the control run results as follows: TWC separates at the Korea/Tsushima Strait into two branches through a western and an eastern channel. Flow through the western channel (i.e., EKWC) closely follows the Korean coast until it separates near 38°N into two branches. The eastern branch follows the SPF to the west coast of Japan, and the western branch, flows northward and forms a cyclonic eddy in the southern UTB. The LCC carries fresh and cool water along the Russian coast and becomes the NKCC at the North Korean coast. The NKCC meets the EKWC at about 38°N. After separation from the coast, the NKCC and the EKWC converge to form a strong zonal jet across the basin.

4.3. Uncertain initial velocity field

As mentioned before, initializing the velocity field with the diagnostic mode (called the diagnostic initialization) contains large uncertainty with the possibility of generating extremely strong thermohaline source/sink terms (Chu and Lan, 2003). Four experiments are designed to investigate the model uncertainty to uncertain initial velocity fields.

Run-1 does not use the velocity initialization. The POM–JES prognostic mode is integrated from

$$\mathbf{V}_0 = 0, \quad T_0 = T_{JD180}, \quad S_0 = S_{JD180}, \quad (6)$$

with the same atmospheric and lateral boundary forcing as the control run (Run-0) for 180 days. Model difference between Run-0 and Run-1 is the uncertainty caused by the zero initial velocity fields.

Run-2, Run-3, and Run-4 are designed to investigate the uncertainty of the diagnostic initialization with various periods. The POM–JES diagnostic mode is integrated from (6) with T_{JD180}, S_{JD180} unchanged for 30, 60, and 90 days to get $\mathbf{V}_{30D}^{(Diag)}$, $\mathbf{V}_{60D}^{(Diag)}$, and $\mathbf{V}_{90D}^{(Diag)}$. The POM-JES prognostic mode is integrated with the same atmospheric and lateral boundary forcing as Run-0 for 180 days from

$$\mathbf{V}_0 = \mathbf{V}_{30D}^{(Diag)}, \quad T_0 = T_{JD180}, \quad S_0 = S_{JD180}, \tag{7}$$

in Run-2; from

$$\mathbf{V}_0 = \mathbf{V}_{60D}^{(Diag)}, \quad T_0 = T_{JD180}, \quad S_0 = S_{JD180}, \tag{8}$$

in Run-3; and from

$$\mathbf{V}_0 = \mathbf{V}_{90D}^{(Diag)}, \quad T_0 = T_{JD180}, S_0 = S_{JD180}, \tag{9}$$

in Run-4 (Table 3).

4.4. Uncertain wind forcing

Two experiments are conducted to investigate the effect of wind uncertainty. Everything remains the same as Run-0 except the monthly mean surface winds where a Gaussian-type random variable added to each COADS wind data point with zero mean and noise intensity of 0.5 m/s for Run-5 and 1 m/s for Run-6, respectively (Table 4). The noise varies in each month.

4.5. Uncertain lateral transport

Two experiments are conducted to investigate the effect of lateral transport uncertainty. Everything keeps the same as Run-0 except the bi-monthly mean lateral boundary transport (see Table 1) where a Gaussian-type random variable is added with the zero mean and noise intensity being 5% and 10% of the transport (control run) for Run-7 and Run-8, respectively (Table 5). The noise varies in 2 months.

4.6. Combined uncertain conditions

Three experiments are conducted to investigate the effect of combined uncertainty (Table 6). Initial conditions remain the same as Run-2 (30 day diagnostic run). For Run-9, the surface wind forcing is the same as Run-6 (1 m/s noise intensity) and the lateral boundary transport is the same as Run-0 (combined uncertainty in winds and initial velocity field). For Run-10, the surface wind is the same as Run-0 (no noise) and the lateral boundary transport is the same as Run-8 (10% noise intensity, combined uncertainty in lateral boundary transport and initial velocity field). For Run-11, the surface wind is the same as Run-6 (1 m/s noise intensity) and the lateral boundary transport is the same as

Table 3
Experiments for uncertain initial conditions

Experiment	Initial conditions	Wind forcing	Lateral boundary transport
1	$\mathbf{V}_0 = 0$, $T_0 = T_{JD180}$, $S_0 = S_{JD180}$	Same as Run-0	Same as Run-0
2	$\mathbf{V}_0 = \mathbf{V}_{30D}^{(Diag)}$, $T_0 = T_{JD180}$, $S_0 = S_{JD180}$	Same as Run-0	Same as Run-0
3	$\mathbf{V}_0 = \mathbf{V}_{60D}^{(Diag)}$, $T_0 = T_{JD180}$, $S_0 = S_{JD180}$	Same as Run-0	Same as Run-0
4	$\mathbf{V}_0 = \mathbf{V}_{90D}^{(Diag)}$, $T_0 = T_{JD180}$, $S_0 = S_{JD180}$	Same as Run-0	Same as Run-0

Table 4
Experiments for uncertain wind forcing

Experiment	Initial conditions	Wind forcing	Lateral boundary transport
5	Same as Run-0	Adding Gaussian random noise with zero mean and 0.5 m/s noise intensity	Same as Run-0
6	Same as Run-0	Adding Gaussian random noise with zero mean and 1.0 m/s noise intensity	Same as Run-0

Table 5
Experiments for uncertain lateral transport

Experiment	Initial conditions	Wind forcing	Lateral boundary transport
7	Same as Run-0	Same as Run-0	Adding Gaussian random noise with the zero mean and noise intensity being 5% of the transport (control run)
8	Same as Run-0	Same as Run-0	Adding Gaussian random noise with the zero mean and noise intensity being 10% of the transport (control run)

Table 6
Experiments for combined uncertainty

Experiment	Initial conditions	Wind forcing	Lateral boundary transport
9	Same as Run-2	Same as Run-6	Same as Run-0
10	Same as Run-2	Same as Run-0	Same as Run-8
11	Same as Run-2	Same as Run-6	Same as Run-8

Run-8 (10% noise intensity), respectively (combined uncertainty in winds, lateral boundary transport and initial velocity field).

5. Statistical error analysis

5.1. Model error measures

Difference between the horizontal velocity $\mathbf{V}$ of control run and each sensitivity run at a σ-level,

$$\Delta\mathbf{V}(x,y,\sigma,t)=\mathbf{V}_c(x,y,\sigma,t)-\mathbf{V}_e(x,y,\sigma,t), \tag{10}$$

is defined as prediction error (PE). Here, the subscripts (c, e) represent the control and sensitivity runs. Temporal evolution of the horizontal mean relative error is represented by the level dependent relative root mean square error (RRMSE) between the control and sensitivity runs

$$R_1(\sigma,t)=\frac{\sqrt{\sum_{i=1}^{Mx}\sum_{j=1}^{My}\{[\Delta u(xi,yj,\sigma,t)]^2+[\Delta v(xi,yj,\sigma,t)]^2\}}}{\sqrt{\sum_{i=1}^{Mx}\sum_{j=1}^{My}\{[u_c(xi,yj,\sigma,t)]^2+[v_c(xi,yj,\sigma,t)]^2\}}}. \tag{11}$$

Temporal evolution of the volume mean relative error is represented by the level-independent RRMSE between the control and sensitivity runs,

$$R_2(t)=\frac{\sqrt{\sum_{i=1}^{Mx}\sum_{j=1}^{My}\sum_{k=1}^{Mz}\{[\Delta u(xi,yj,\sigma_k,t)]^2+[\Delta v(xi,yj,\sigma_k,t)]^2\}}}{\sqrt{\sum_{i=1}^{Mx}\sum_{j=1}^{My}\sum_{k=1}^{Mz}\{[u_c(xi,yj,\sigma_k,t)]^2+[v_c(xi,yj,\sigma_k,t)]^2\}}}. \tag{12}$$

6. JES model predictability

Level dependent and independent RRMSEs, $R_1(\sigma,\ t)$ and $R_2(t)$, are calculated for all the experiments. Typical values of RRMSE are listed in Table 7.

6.1. Predictability of the first kind

The first kind predictability is due to uncertain initial condition. Level dependent RRMSE, $R_1(\sigma,\ t)$, varies with time with larger values on the 5th day (0.45–0.75, Fig. 4a) than on the 180th day (0.20–0.27, Fig. 4b). Level dependence of $R_1(\sigma,\ t)$ also changes with time from maximum error at the bottom on the 5th day (0.60–0.75) to near surface on the 180th day (near 0.25). Level independent RRMSE, $R_2(t)$, rapidly decreases with time in the first 20 days from a peak value of 0.5 to 0.3 and then slowly decreases with time to 0.2 on the 180th day (Fig. 5). There is little difference in $R_1(\sigma,\ t)$ and $R_2(t)$ in the four sensitivity runs (Figs. 4 and 5), indicating

Table 7
RRMSEs in various experiments

Experiment	Level independent RRMSE, $R_2(t)$		Maximum of level dependent RRMSE, $R_1(\sigma, t)$	
	Min. (%)	Max. (%)	5th day	180th day
Uncertain initial velocity	20	50	70% near the surface	25% near the surface
Uncertain winds with 0.5 m/s noise intensity	8	19	35% near the surface	50% near the surface
Uncertain winds with 1.0 m/s noise intensity	11	28	60% near the surface	80% near the surface
Uncertain lateral boundary transport with 5% noise intensity	9	20	14% near the bottom	18% near the bottom
Uncertain lateral boundary transport with 10% noise intensity	17	34	24% near the bottom	28% near the bottom
Uncertain initial velocity (30 days of diagnostic run) and wind forcing (1 m/s noise)	20	52	70% near the surface	77% near the surface
Uncertain initial velocity (30 days of diagnostic run) and lateral boundary transport (10% noise)	27	50	65% near the bottom	35% near the bottom
Uncertain initial velocity (30 days of diagnostic run), wind forcing (1 m/s noise) and lateral boundary transport (10% noise)	30	55	73% near the surface	78% near the surface

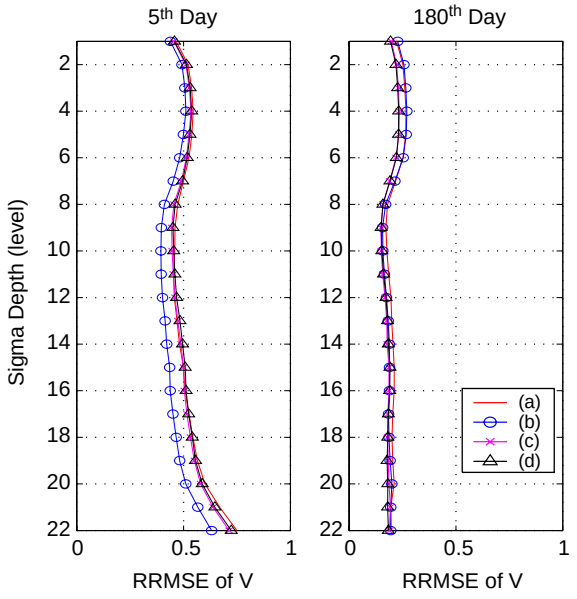

Fig. 4. Level dependent RRMSE due to uncertain initial velocity field without diagnostic initialization (Run 0–Run 1, represented by the solid curve), with diagnostic initialization for 30 day period (Run 0–Run 2, represented by the symbol '○'), for 60 day period (Run 0–Run 3, represented by the symbol 'X'), and for 90 day period (Run 0–Run 4, represented by the symbol 'Δ') on the (a) 5th day and (b) 180th day after the model integration.

no difference using and not using the diagnostic (velocity) initialization and no difference in choosing periods (30–90 days) for diagnostic initialization.

6.2. *Predictability of the second kind*

The second kind predictability is due to uncertain wind forcing and/or lateral transport (Chu, 1999).

6.2.1. *Due to uncertain wind forcing*

The level dependent RRMSE, $R_1(\sigma, t)$, varies with time with smaller values on the 5th day (Fig. 6a) than on the 180th day (Fig. 6b). It increases with the noise intensity for the same (σ, t), reduces drastically from a maximum value at the surface (0.35 for noise intensity of 0.5 m/s and 0.50 for noise intensity of 1 m/s on the 5th day, and 0.60 for noise intensity of 0.5 m/s and 0.80 for noise intensity of 1 m/s on the 180th day) to a smaller value at the sigma level-8 (0.08 for noise intensity of 0.5 m/s and 0.10 for noise intensity of 1 m/s on the 5th day, and 0.10 for noise intensity of 0.5 m/s and 0.18 for noise intensity of 1 m/s on the 180th day), and then changes slightly with level to the bottom. This indicates that the level dependent RRMSE due to the wind error has maximum value at the surface, decreases with level, and increases from 5th to 180th day.

Level independent RRMSE (Fig. 7), $R_2(t)$, increases with time slowly in the first 45 days (0.12 with wind noise intensity of 0.5 m/s and 0.20 with wind noise intensity of 1.0 m/s)., decreases with time from the 45th day to 0.08 (wind noise intensity of 0.5 m/s) and 0.12 (wind noise intensity of 1.0 m/s) at the 60th day, and then increases with time to the

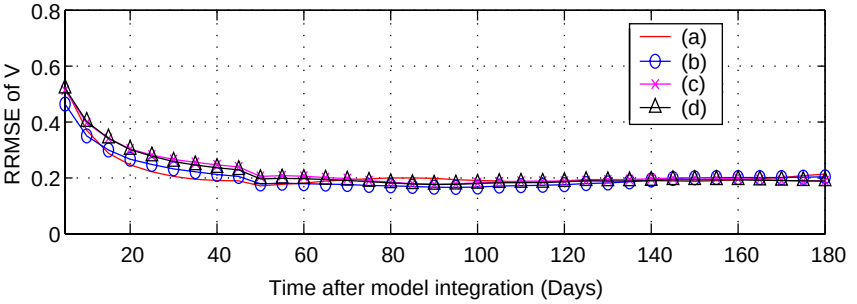

Fig. 5. Temporal evolution of the level independent RRMSE due to uncertain initial velocity field. Note that there is little difference among the four cases.

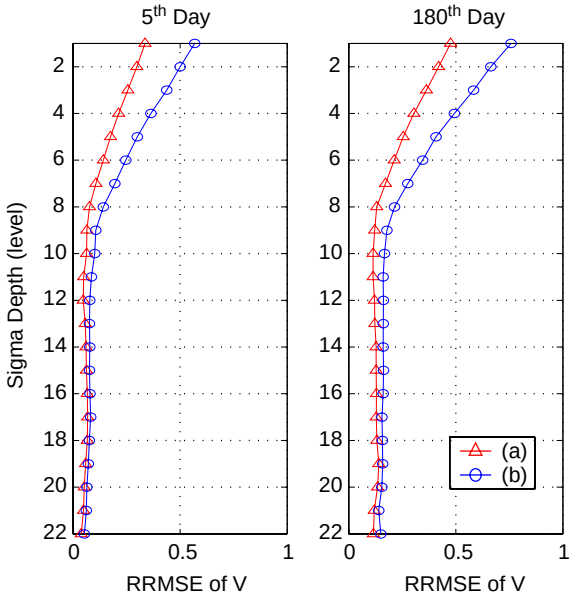

Fig. 6. Level dependent RRMSE due to uncertain wind forcing with 0.5 m/s noise intensity (Run 0–Run 5, represented by the symbol 'Δ') and 1.0 m/s noise intensity (Run 0–Run 6, represented by the symbol '○') on the (a) 5th day and (b) 180th day after the model integration.

180th day and reaches the maximum values: 0.19 (wind noise intensity of 1.0 m/s) and 0.28 (wind noise intensity of 1.0 m/s).

6.2.2. *Due to uncertain lateral transport*

The level-dependent RRMSE, $R_1(\sigma, t)$, varies with time with smaller values on the 5th day (Fig. 8a) than on the 180th day (Fig. 8b). It increases with the noise intensity for the same (σ, t), and increases from a minimum value at the surface (0.05 for 5% noise intensity and 0.08 for 10% noise intensity on the 5th day, and 0.10 for 5% noise intensity and 0.15 for 10% noise intensity on the 180th day) to a maximum value at the bottom (0.16 for 5% noise intensity and 0.23 for 10% noise intensity on the 5th day, and 0.18 for 5% noise intensity and 0.28 for 10% noise intensity on the 180th day). Level independent RRMSE, $R_2(t)$, oscillates with time with smaller values (0.09–0.20) for 5% noise intensity and with larger values (0.17–0.34) for 10% noise intensity (Fig. 9).

6.2.3. *Major features*

Several major features are found for the second kind predictability of the JES–POM model. First, the model uncertainty enhances with the increase of the noise intensity. Second, the model error decreases with the level due to the wind uncertainty (Fig. 6), and increases with the level due to the lateral transport uncertainty (Fig. 8). The overall model uncertainty (i.e., $R_2(t)$) has error growth stage (evident in the wind uncertainty, Fig. 7) and oscillatory stage (evident in the lateral transport uncertainty, Fig. 9).

Chu (1999) found the two stages of error growth in the second kind predictability of the Lorenz system: a growing stage and followed by an oscillation stages. During the growing stage, the model error increases with time. During the oscillation stage, the model error oscillates between two evident values. The model error usually decreases with time between the growth and oscillatory stages. In the JES–POM model, the second kind predictability also has two stages. However, the oscillatory stage due to the wind uncertainty (Fig. 7) is not as evident as that due to the lateral transport uncertainty (Fig. 9).

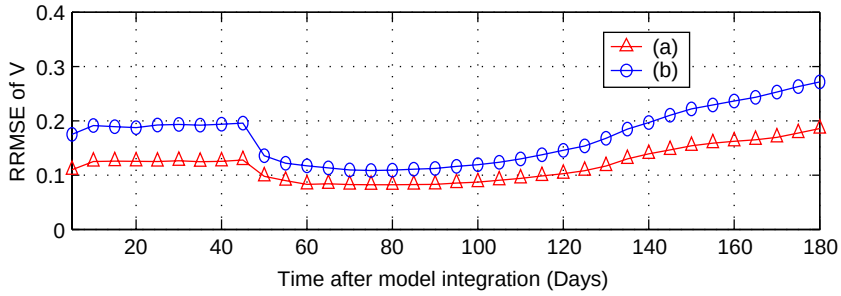

Fig. 7. Temporal evolution of level independent RRMSE due to uncertain winds with the symbol 'Δ' denoting 0.5 m/s noise intensity and the symbol '○' representing 1.0 m/s noise intensity. Note that the error oscillates with an evident error-growing trend.

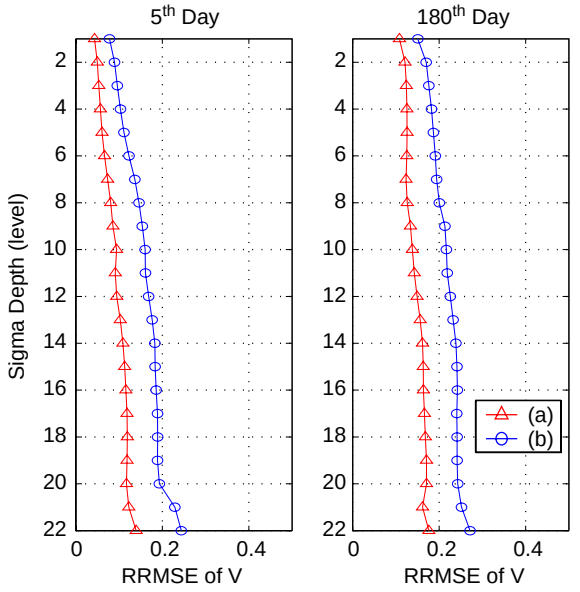

Fig. 8. Level dependent RRMSE due to uncertain lateral boundary transport with 5% noise intensity (Run 0–Run 7, represented by the symbol 'Δ') and 10% noise intensity (Run 0–Run 8, represented by the symbol '○') on the (a) 5th day and (b) 180th day after the model integration.

6.3. *Due to combined uncertain conditions*

Different types of input uncertainty lead to various error evolutions. The model RRMSE deceases with time for uncertain initial velocity, oscillates with an evident error-growing trend for uncertain wind forcing, and oscillates without an evident error-growing trend for uncertain lateral boundary transport. Usually, ocean models contain different types of input uncertainties.

$R_1(\sigma, t)$ for three combined uncertainty runs (Runs 9–11) is illustrated for the 5th day (Fig. 10a) and the 180th day (Fig. 10b). It has little difference among all the three cases below the sigma level-8 and between Run-9 (combined uncertain initial velocity and winds) and Run-11 (combined uncertain initial velocity, winds, and lateral boundary transport) above the sigma level-8 with a maximum value at the surface: 0.73 for the 5th day and 0.78 for the 180th day. At the lower level (below the sigma level-8), it reduces from the 5th day (~0.65 at the bottom) to the 180th day (~0.35 at the bottom). At the upper layer (above the sigma level-8), it is smaller without wind errors (Run-10) than with wind errors (Run-9 and Run-11). The RRMSE at the surface is 0.45 for the 5th day and 0.24 for the 180th day.

Level independent RRMSE, $R_2(t)$, oscillates with time between 0.20 and 0.52 for combined uncertain initial velocity and winds, 0.27 and 0.50 for combined uncertain initial velocity and lateral boundary transport, and 0.30 and 0.55 for combined uncertain initial velocity, winds, and lateral boundary transport (Fig. 11).

7. Discussion of the results

Predictability of the first kind is the model uncertainty due to initial velocity uncertainty. Keeping wind forcing and open boundary condition accurate, and initial velocity field is changed from 'accurate condition' ((5) for the control run) to 'perturbed conditions' represented by various velocity initialization schemes ((6)–(9) for the sensitivity runs). The predictability of the first kind due to various velocity initialization schemes is investigated from comparison between the control and sensitivity runs and has the following features: (1) there is no difference using and not using the diagnostic (velocity) initialization; (2) there is no

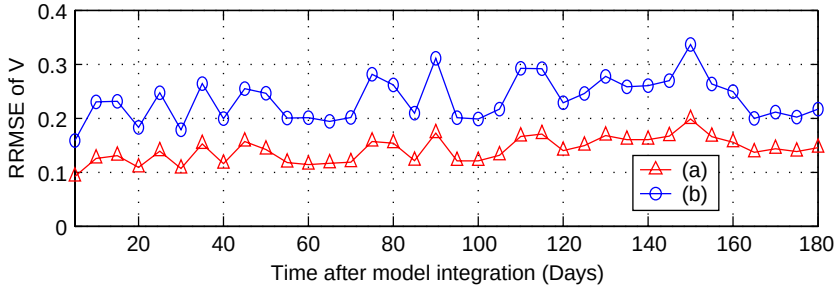

Fig. 9. Temporal evolution of level independent RRMSE due to uncertain lateral boundary transport with the symbol 'Δ' denoting 5% noise intensity and the symbol '○' representing 10% noise intensity. Note that the error oscillates with no evident error-growing trend.

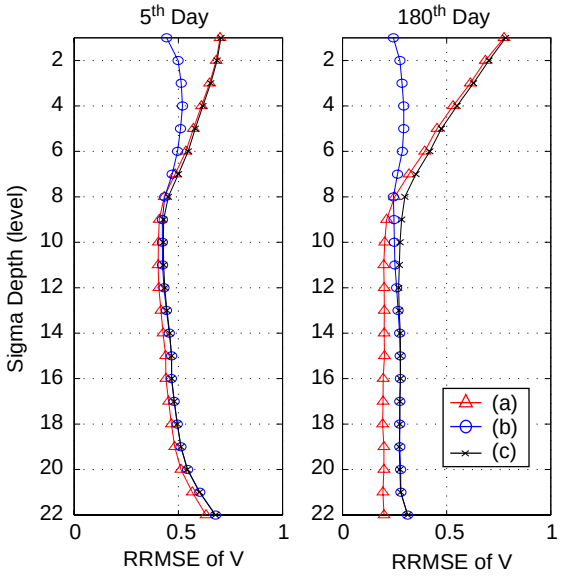

Fig. 10. Level dependent RRMSE due to uncertain initial velocity and surface winds (Run 0–Run 9, represented by the symbol 'Δ'), uncertain initial velocity and lateral boundary transport (Run 0–Run 10, represented by the symbol '○'), and uncertain initial velocity, winds and lateral boundary transport (Run 0–Run 11, represented by the symbol 'X') on the (a) 5th day and (b) 180th day after the model integration.

difference in choosing periods (30–90 days) for diagnostic initialization, and (3) the level independent RRMSE reaches a steady value (0.2 in Fig. 5). This shows that the commonly used zero-velocity and diagnostic initialization schemes are equivalent and non-realistic. A velocity field $\mathbf{V}_0$, which is dynamically consistent with the initial conditions (T_0, S_0), should be used as the initial velocity condition. One possibility is to use the absolute geostrophic velocity calculated using the *P*-vector method (Chu, 1995).

Predictability of the second kind is the model uncertainty due to wind forcing/open boundary conditions. Keep the initial condition (3) accurate, and perturb the wind forcing (2) and open boundary condition (4) with white noises. The predictability of the second kind due to uncertain winds (Figs. 6 and 7) and uncertain lateral boundary conditions (Figs. 8 and 9) has the following features: (1) the model error increases with the noise intensity, (2) the model error decreases with the depth from a maximum value at the surface and a minimum value at the bottom; and (3) the level independent RRMSE generally increases with time (especially shown in Fig. 7).

Different characteristics in the JES model predictability is found between the first kind (general decrease of RRMSE with time) and the second kind (general increase of RRMSE with time). Such difference may be caused by the different types of noise addition. For the predictability of the first kind, the uncertainty only exists at the one time instance (i.e., the initial conditions). However, for the predictability of the second kind, the noise is added to the winds/lateral boundary conditions at any time instance. Increase of RRMSE in the predictability of the second kind (with uncertain winds) in the South China Sea prediction system (based on the POM model) was also reported by Chu et al. (1999).

8. Conclusions

(1) Model uncertainty due to uncertain initial velocity field reduces with time. Level independent RRMSE rapidly decreases with time in the first 20 days from a peak value of 0.5–0.3 and then slowly decreases with time to 0.2 on the 180th day. There is no difference using and not

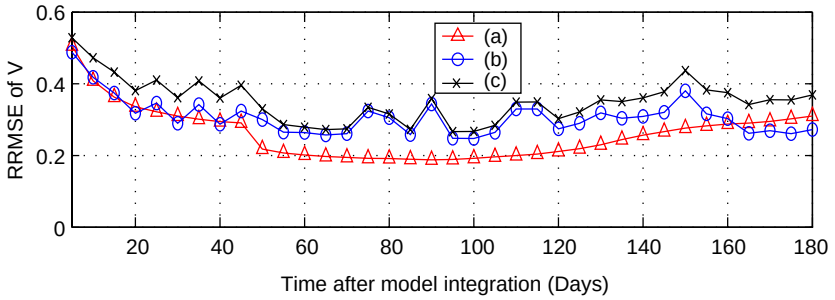

Fig. 11. Temporal evolution of level independent RRMSE due to uncertain initial velocity and surface winds (represented by the symbol 'Δ'), uncertain initial velocity and lateral boundary transport (represented by the symbol '○'), and uncertain initial velocity, winds and lateral boundary transport (represented by the symbol 'X').

using the diagnostic (velocity) initialization and no difference in choosing periods (30–90 days) for diagnostic initialization.

(2) Model uncertainty due to uncertain winds increases with the wind noise intensity. RRMSE oscillates with an evident error growing trend and reduces with level. It has a maximum value of 0.60 (0.80) for 0.5 m/s (1 m/s) noise intensity at the surface on 180th day. Level independent RRMSE reaches 0.19 (0.28) for noise intensity of 0.5 m/s (1.0 m/s).

(3) Model uncertainty due to uncertain lateral boundary transport increases with the transport noise intensity. RRMSE oscillates with no evident error-growing trend. It has a maximum value of 0.18 (0.28) for 5% (10%) noise intensity at the bottom 180th day. Level independent RRMSE reaches 0.20 (0.34) for noise intensity of 5% (10%).

(4) Model uncertainty due to combined uncertain initial velocity field (30 day diagnostic period), winds with noise intensity of 1 m/s, and lateral boundary transport with noise intensity of 10% has a maximum value at the surface: 0.73 for the 5th day and 0.78 for the 180th day. Level independent RRMSE oscillates with time between 0.20 and 0.52 for combined uncertain initial velocity and winds, 0.27 and 0.50 for combined uncertain initial velocity and lateral boundary transport, and 0.30 and 0.55 for combined uncertain initial velocity, winds, and lateral boundary transport.

(5) Model uncertainty due to uncertain input data (initial velocity, winds, and lateral boundary transport) is significant. It is urgent to reduce the input uncertainties for achieving accurate prediction of the ocean behavior and to study the ocean predictability. Similar to the Lorenz system, the second kind predictability of the JES-POM model also has two stages: error growth and oscillatory stages. In the JES-POM model, the second kind predictability also has two stages. However, the oscillatory stage due to the wind uncertainty is not as evident as that due to the lateral transport uncertainty. The physical mechanisms causing such difference need to be further explored.

(6) A Gaussian-type random noise is added to the COADS $1^\circ \times 1^\circ$ monthly mean wind field (once a month) and to the bi-monthly lateral transport (not on grid). Such uncertainty might not be the same as in reality. Usually, the surface wind varies from day to day at a spatial scale of 10–100 km. Therefore, the monthly wind on $1^\circ \times 1^\circ$ resolution and bi-monthly mean transports are too smooth. The random noises added to these mean fields are also too smooth spatially and temporally.

References

Bang, I., Choi, J.-K., Kantha, L., Horton, C., Cliford, M., Suk, M.-S., Chang, K.-I., Nam, S.Y., Lie, H.-J., 1996. A hindcast experiment in the East Sea (Sea of Japan). La mer 34, 108–130.

Blumberg, A., Mellor, G., 1987. A description of a three dimensional coastal ocean circulation mode. In: Heaps, N.S. (Ed.), Three-Dimensional Coastal Ocean Models. American Geophysics Union, Washington, DC, pp. 1–16.

Chapman, D., 1985. Numerical treatment of cross-shelf open boundaries in a barotropic ocean model. Journal of Physical Oceanography 15, 1060–1075.

Chu, P.C., 1995. *P* vector method for determining absolute velocity from hydrographic data. Marine Technology Society of Japan 29 (2), 3–14.

Chu, P.C., 1999. Two kinds of predictability in Lorenz system. Journal of the Atmospheric Sciences 56, 1427–1432.

Chu, P.C., Lan, J., 2003. Extremely strong thermohaline source/sinks generated by diagnostic initialization. Geophysical Research Letters 30 (6).

Chu, P.C., Fan, C.W., Ehret, L.L., 1997. Determination of open boundary conditions with an optimization method. Journal of the Atmospheric and Oceanic Technology 14, 723–734.

Chu, P.C., Chen, Y.C., Lu, S.H., 1998. Temporal and spatial variabilities of Japan Sea surface temperature and atmospheric forcings. Journal of Oceanography 54, 273–284.

Chu, P.C., Lu, S.H., Liu, W.T., 1999. Uncertainty of South China Sea prediction using NSCAT and national centers for environmental prediction winds during tropical storm Ernie, 1996. Journal of Geophysical Research 104, 11273–11289.

Chu, P.C., Lan, J., Fan, C.W., 2001a. Japan/East Sea thermohaline structure and circulation, Part 1, Climatology. Journal of Physical Oceanography 31, 244–271.

Chu, P.C., Lan, J., Fan, C.W., 2001b. Japan/East Sea thermohaline structure and circulation, Part 2, A variational P-vector method. Journal of Physical Oceanography 31, 2886–2902.

Chu, P.C., Lu, S.H., Fan, C.W., Kim, C.S., 2003. A numerical simulation on Japan/East Sea thermohaline structure and circulation. In: Lakhan, V.C. (Ed.), Advances in Coastal Modeling, vol. 67. Elsevier Oceanography Series.

Fang, C.L., 2003. Predictability of Japan/East Sea (JES) system to uncertain initial/lateral boundary conditions and surface winds. M.S. Thesis, Naval Postgraduate School, Monterey, CA, 79pp.

Gong, Y., Park, C.G., 1969. On the oceanographical character of the low temperature region in the eastern sea of Korea. Bull. Fish. Res. Dev. Agency, Korea. 4, 69–91.

Gordon, A.L., Giulivi, C.F., Lee, C.M., Furey, H.H., Bower, A., Tally, L., 2002. Japan/East Sea interthermocline eddies. Journal of Physical Oceanography 32, 1960–1974.

Hogan, P.J., Hurlburt, H.E., 2000. Impact of upper ocean topographical coupling and isopycnal outcropping in Japan/East Sea models with 1/8 to 1/64 resolution. Journal of Physical Oceanography 30, 2535–2561.

Holloway, G.T., Sou, T., Eby, M., 1995. Dynamics of circulation of the Japan Sea. Journal of Marine Research 53, 539–569.

Isoda, Y., Saitoh, S., 1993. The northward intruding eddy along the east coast of Korea. Journal of Oceanography 17, 265–276.

Isoda, Y., Saitoh, S., Mihara, M., 1991. SST structure of the polar front in the Japan Sea. In: Yakano, K. (Ed.), Oceanography of Asian Marginal Seas. Elsevier, Amsterdam, pp. 103–112.

Kim, C.-H., Yoon, J.-H., 1996. Modeling of the wind-driven circulation in the Japan Sea using a reduced gravity model. Journal of Oceanography 52, 359–373.

Kim, K., Chung, J.Y., 1984. On the salinity-minimum layer and dissolved oxygen-maximum layer in the East Sea (Japan Sea). In: Ichiye, T. (Ed.), Ocean Hydrodynamics of the Japan and East China Sea. Elsevier, Amsterdam, pp. 55–65.

Kim, Y.G., Kim, K.K., 1999. Intermediate waters in the East/Japan Sea. Journal of Oceanography 55, 123–231.

Martin, S., Kawase, M., 1998. The southern flux of sea ice in the Tatarskiy Strait, Japan Sea and the generation of the Liman Current. Journal of Marine Research 56, 141–155.

Miyazaki, M., 1953. On the water masses of the Japan Sea. Bull. Hokkaido Reg. Fisher. Res. Lab. 7, 1–65 (in Japanese with English abstract).

Moriyasu, S., 1972. The Tsushima Current. In: Stommel, H., Yoshida, K. (Eds.), Kuroshio—Its Physical Aspects. University of Tokyo Press, Tokyo, pp. 353–369.

Preller, R.H., Hogan, P.J., 1998. Oceanography of the Sea of Okhotsk and the Japan/East Seas. In: Robinson, A.R., Brink, K.K. (Eds.), The Sea, vol. 11. Wiley, New York, pp. 429–481.

Senjyu, T., 1999. The Japan Sea intermediate water: its characteristics and circulation. Journal of Oceanography 55, 111–122.

Seung, Y.H., Kim, K., 1989. On the possible role of local thermal forcing on the Japan Sea circulation. Journal of the Oceanological Society of Korea 24, 1–14.

Shin, H.-R., Byun, S.-K., Kim, C., 1995. The characteristics of structure of warm eddy observed to the northwest of Ulleungdo in 1992. Journal of the Oceanological Society of Korea 30, 39–56.

Shin, C.W., Byun, S.K., Kim, C.S., 1996. Comparison between geostrophic currents in the southwestern part of the East Sea. Journal of the Oceanological Society of Korea 31, 89–96.

Spall, M.A., 2002. Wind- and buoyancy-forced upper ocean circulation in two-strait marginal seas with application to the Japan/East Sea. Journal of Geophysical Research 107.

Toba, Y., Tomizawa, K., Kurasawa, Y., Hanawa, K., 1982. Seasonal and year-to-year variability of the Tsushima–Tsugaru Warm Current system with its possible cause. La mer 20, 41–51.

Yi, S.U., 1966. Seasonal and secular variations of the water volume transport across the Korea Strait. Journal of the Oceanographical Society of Korea 1, 7–13.

Yoon, J.-H., 1982. Numerical experiment on the circulation in the Japan Sea, part I, Formation of the East Korean Warm Current. Journal of Oceanographical Society of Japan 38, 43–51.